Graphene: synthesis and applications

Graphene, since the demonstration of its easy isolation by the exfoliation of graphite in 2004 by Novoselov, Geim and co-workers, has been attracting enormous attention in the scientific community. Because of its unique properties, high hopes have been placed on it for technological applications in many areas. Here we will briefly review aspects of two of these application areas: analog electronics and photonics/optoelectronics. We will discuss the relevant material properties, device physics, and some of the available results. Of course, we cannot rely on graphite exfoliation as the source of graphene for technological applications, so we will start by introducing large scale graphene growth techniques.

Phaedon Avouris* and Christos Dimitrakopoulos
IBM Research Division, T.J. Watson Research Center, Yorktown Heights, NY 10598, USA
*E-mail: avouris@us.ibm.com

The low energy bandstructure of graphene involves its π electrons. The first bandstructure calculations were performed in 1947 by P.R. Wallace[1] and the bandstructure is shown in Fig. 1a. The valence band is formed by bonding π states, while the conduction band is formed by the anti-bonding π* states. These states are orthogonal; there is no avoided crossing, and valence and conduction bands touch at six points, the so-called Dirac points. Two of these points are independent and are indicated in Fig. 1a as the K and K' points. For energies below about 1 eV, which are relevant in most electrical transport properties, the bandstructure can be approximated by two symmetric cones representing valence and conduction bands touching at the Dirac point. Electron dispersion in this energy region is to a large extent linear, similar to that of light and unlike other conventional 2D systems with parabolic dispersion[2-8]. This linear dispersion has profound implications regarding the properties of graphene. Also, unlike the conventional 2D electron systems, which

are usually formed at buried semiconductor interfaces, graphene is a single atomic layer directly accessible to experimental observation, but also very susceptible to external perturbations which can interact directly with its π-electron system.

The unit cell of graphene contains two carbon atoms and the graphene lattice can be viewed as formed by two sub-lattices, A and B, evolving from these two atoms (see Fig. 1b). The electronic Hamiltonian describing the low energy electronic structure of graphene can then be written in the form of a relativistic Dirac Hamiltonian: $H = v_F\sigma \cdot \hbar k$, where σ is a spinor-like wavefunction, v_F is the Fermi velocity of graphene, and k the wavevector of the electron[2-8]. However, the spinor character of the graphene wavefunction arises not from spin, but from the fact that there are two atoms in the unit cell. We can define a pseudo-spin that has the same direction as the group velocity and describes the electron population in the A and B sites. As with real spin, pseudo-spin reversal is not allowed during carrier interactions. This underlies the inhibition of
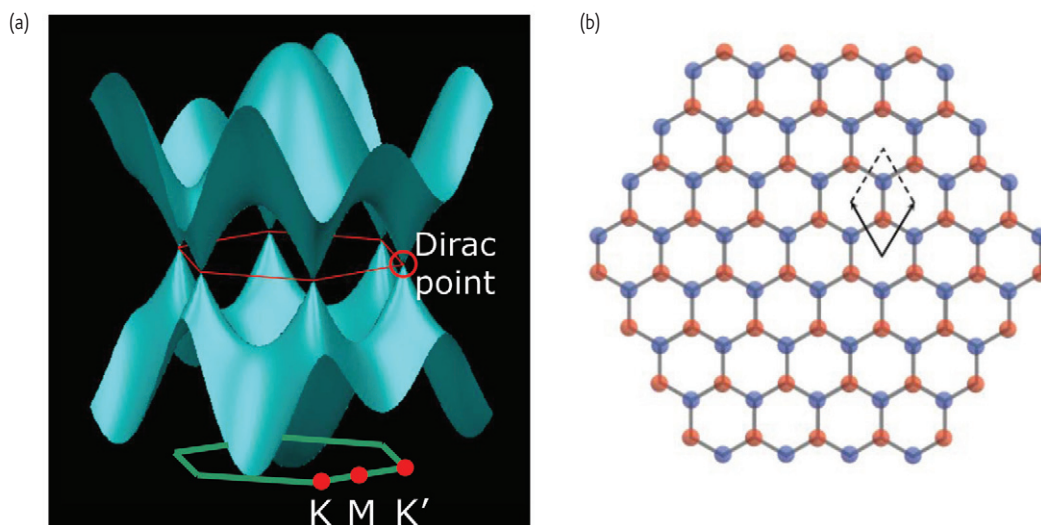
Fig. 1 (a) Representation of the electronic bandstructure and Brillouin zone of graphene. (b) The two graphene sub-lattices (red and blue) and unit cell.

backscattering in graphene[2-8]. The inhibition of backscattering, the weak electron-phonon coupling and the high optical phonon frequencies are responsible for the outstanding transport properties of graphene.

Graphene synthesis

Graphene has been synthesized in various ways and on different substrates. In the following, we summarize the synthesis methods, and comment on their maturity, advantages and disadvantages, and targeted applications.

Graphene was first exfoliated mechanically from graphite in 2004[9]. This simple, low-budget technique has been widely credited for the explosive growth of interest in graphene. Graphene flakes have been invaluable to the study and elucidation of graphene properties. Unfortunately, however, they are usually available at a size of several-microns (or tens of microns at best), have irregular shapes, and their azimuthal orientation is not deterministically controlled. Technological applications that take advantage of graphene's extraordinary electronic transport properties require structurally coherent graphene on a large scale (e.g., wafer-scale), or large arrays of graphene flakes positioned with a unique azimuthal orientation on a substrate. The latter structures have not yet been demonstrated with flakes and this technology is expected to have limited relevance to commercial high-end electronic applications. Below, we focus mainly on graphene synthesis techniques that have shown promise for circumventing the aforementioned limitations.

Graphene and few-layer graphene (FLG) have been grown by chemical vapor deposition (CVD) from C-containing gases on catalytic metal surfaces and/or by surface segregation of C dissolved in the bulk of such metals. Depending on the solubility of C in the metal, the former or the latter can be the dominant growth process, or they can coexist.

The first evidence of "single layer graphite" on metals was found in low energy electron diffraction (LEED) patterns from Pt surfaces[10].

These patterns were correctly attributed to "surface carbon" segregated at the surface from the bulk of Pt crystals[11], but were first interpreted specifically as single layer graphite by J. W. May in 1969[12]. A lot of work has been devoted since to the study of the formation of single or few layer graphite by surface segregation of C during annealing of various C-doped metals, including Ni[13], Fe[14], Pt[15], Pd[15], and Co[15]. An example of the coexistence of CVD and surface segregation processes can be found in the graphitization of Ni in a CH_4-H_2 mixture at $\geq$ 1000 °C[16,17], where the production of carbon species at the Ni surface by the decomposition of CH_4 creates a concentration gradient between the surface and the bulk, causing carbon atoms to diffuse into the metal and form a solid solution. After saturation, graphite forms on the surface. Upon cooling, C atoms dissolved in the metal at high temperature precipitate out and segregate at the metal surface, forming more layers of graphene. This process is difficult to control, especially on polycrystalline metal foils, in which the grain boundaries behave differently than the grains[18]. In single crystal Ni (111), the atomically smooth surface and the absence of grain boundaries produce more uniform and thinner FLG, while in polycrystalline Ni, grain boundaries serve as graphene nucleation sites favoring multilayer growth. Different cooling rates lead to different C segregation behaviors, affecting the thickness and quality of graphene films[19]. Annealing the Ni surface in H_2 before graphene formation is beneficial to the thickness uniformity of the graphene layer[19]. H_2 eliminates impurities such as S and P that cause local variations of carbon solubility, affecting the local graphene thickness[17]. Reina et al.[20] used ambient-pressure CVD to synthesize 1 − 12 layer graphene films on polycrystalline Ni films, while ethylene decomposition on Pt(111) surfaces, resulted in the formation of a single layer of epitaxial graphite[21].

The deposition of graphene on Cu surfaces provides a good example of a purely surface-mediated CVD process[22]. The solubility of C in Cu is minimal (less than 0.001 atom% at 1000 °C[23] vs. 1.3 atom% at 1000 °C in pure Ni[24]), thus graphene can form on Cu only by direct decomposition

of the C containing gas on the catalytic Cu surface. The graphene growth process is self-limiting[23], practically stopping at one monolayer (ML). Such control is very difficult in the case of graphene grown on Ni, due to the considerable solubility of C in Ni. Graphene has also been grown epitaxially on Ru(0001) by surface segregation[25,26] and on Ir(111) by low-pressure CVD[27,28].

The electrical properties of CVD graphene cannot be tested *in situ* on the conductive metal substrates. Thus, processes to transfer graphene on an appropriate insulating substrate have been developed[19,20,22]. The ability to select the host substrate independently of the sacrificial growth substrate is a major advantage for graphene grown on metals. At the same time, the transfer process often affects negatively graphene's integrity, properties, and performance. Wrinkle formation, impurities, graphene tearing, and other structural defects, can occur during transfer. Graphene growth on (not necessarily flat) substrates with sizes limited only by the size of the reactor, or in a continuous roll-to-roll process[29], enables graphene production at a large scale and lowers the cost per unit area. This will potentially enable several large area applications of graphene in the future (e.g., transparent electrodes for large area electronics and solar cells as ITO replacement)[30].

Although graphene grows epitaxially on most metals, on polycrystalline metal substrates it has a polycrystalline structure in 2D, i.e., within the same graphene layer there are single crystal domains of graphene azimuthally rotated relative to neighboring domains and stitched together with defective domain boundaries, such as alternating pentagon-heptagon structures[31]. CVD graphene grown on Cu has the advantage of an almost exact one ML growth, as discussed above, but even when it is grown on single crystal Cu, it still has a multidomain structure, because of the rotational disorder between domains and the many grain boundaries[32,33]. A strict epitaxial relation between the graphene and Cu lattices has yet to be proven (or disproven)[34]. However, under the appropriate conditions, large single crystals of graphene can be grown, as shown on Fig. 2a[35].

While CVD graphene may exhibit electrical transport properties similar to those of exfoliated graphene flakes (e.g., high mobility) when the measurement takes place within a single graphene domain, interdomain measurements show the effects of the grain boundaries. This may explain the variability in mobility often observed in CVD graphene. When it comes to high-end applications, where mobility maximization and uniformity is required at the wafer scale, techniques that may produce graphene with a unique azimuthal orientation over a whole wafer are pursued. In the following we discuss the approach based on SiC.

The graphitization of hexagonal SiC crystals during annealing at high temperatures *in vacuo* was reported by Badami as early as 1961[36]. Under such annealing conditions the top layers of SiC crystals undergo thermal decomposition, Si atoms desorb and the carbon atoms remaining on the surface rearrange and re-bond to form epitaxial graphene layers[37-39]. The kinetics of graphene formation as well as the resulting graphene structure and properties depend on the reactor pressure and the type of gas atmosphere[40-47]. Growth on the Si-face of hexagonal SiC wafers, i.e., h-SiC(0001), under appropriate conditions exhibits manageable growth kinetics (contrary to the C-face growth) allowing better control over the number of graphene layers. This, coupled with the fact that the azimuthal orientation of epitaxial graphene on the Si-face is determined by the crystal structure of the substrate[37,38], provides a pathway towards uniform coverage and structural coherence at wafer-scale. In addition, graphene grown on semi-insulating SiC can be used *in situ* without transfer to another insulating substrate.

Graphene formation starts at the top surface layers of SiC and proceeds inwards[48,49]. Approximately three Si-C bilayers decompose (ca. 0.75 nm) to form one graphene layer (ca. 0.34 nm). A C-rich $(6\sqrt{3}\times6\sqrt{3})R30°$ surface reconstruction (called a "buffer layer") forms initially, where the C atoms are arranged isostructurally to graphene but there is no sp^2 structure and covalent bonds to underlying Si atoms still exist[48]. This layer is insulating and does not exhibit the electronic
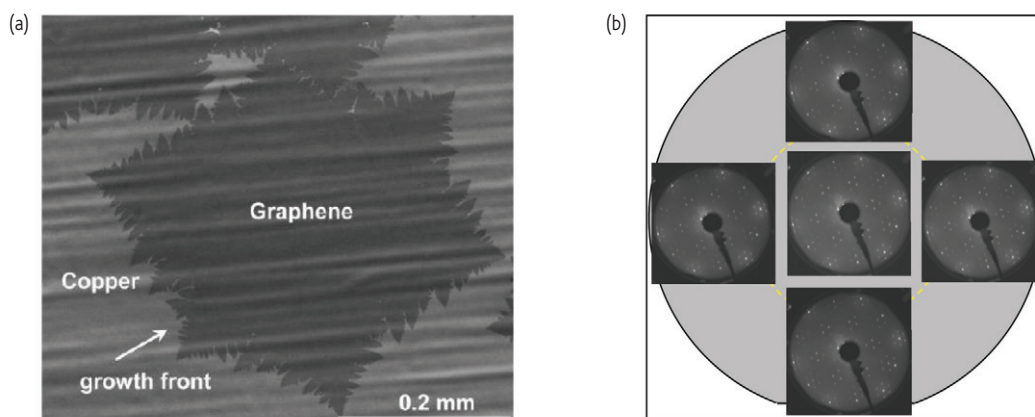

(a)

(b)

Fig. 2 (a) Single crystal of CVD graphene on Cu. Reprinted with permission from[35]. © 2011 American Chemical Society. (b) LEED patterns of epitaxial graphene on a 2 inch SiC wafer, taken at various spots on the wafer. The patterns are practically identical, and the azimuthal orientation is the same anywhere we looked on the wafer. Graphene was grown with the following process: Annealing at 810 °C in UHV for about 45 min, followed by annealing under flow of 20 % disilane in He at 810 and 1140 °C for 10 min at each temperature, followed by graphenization at 1550 °C for 10 min under Ar flow at a pressure of 3.5 mTorr (from reference[52]).

properties of graphene. Subsequently, a new buffer layer forms below the original one that is simultaneously converted to graphene. The buffer layer is responsible for the *n* type doping of pristine graphene on SiC (0001). A second graphene layer can grow in the same way. The rate of graphene formation slows down dramatically after the second layer[41]. This is attributed to the inhibition of Si removal from the buried SiC decomposition front. Si atoms have to diffuse to a defect in graphene (e.g., a pinhole or grain boundary), a SiC terrace edge, or the sample edge, in order to escape. More graphene layers form when graphene defectivity increases. In high vacuum, graphenization starts at relatively low temperatures (1100 – 1200 °C), where C atoms are not adequately mobile and defective graphene films with variable thickness up to ~ 6 layers are formed on a heavily pitted SiC surface[50,51]. In an inert gas atmosphere (e.g., Ar) at pressures up to 1 bar, the sublimation rate of Si is reduced dramatically, and graphenization starts at temperatures higher than 1450 – 1500 °C, where C atoms are more mobile and form higher

quality graphene films with a thickness limited to only ~ 1 – 2 layers[44]. The lower thickness is likely the result of the small concentration of graphene defects, which otherwise would have acted as escape routes for Si atoms.

The structural coherence at wafer-scale of epitaxial graphene on h-SiC(0001) is demonstrated in Fig. 2b[52], which shows five practically identical LEED patterns, obtained at different wafer areas. This sample was grown using an optimized multistep growth process comprising surface preparation in disilane and graphenization in Ar[52,53]. Samples grown with this process exhibit Hall mobilities approaching 5000 cm^2/Vs at a carrier density n ≈ 4 × 10^{11} cm^{-2}.[54]

Fig. 3a[55] is an AFM height image of a vicinal SiC surface after H$_2$ etching at 1555 °C. H$_2$ etches the top layers of SiC that might have been damaged during wafer fabrication[56]. Fig. 3b is an AFM image of graphene grown at 1575 °C under Ar flow on H$_2$ etched SiC. The surface is pit-free and the terrace width has increased dramatically due to vicinal step
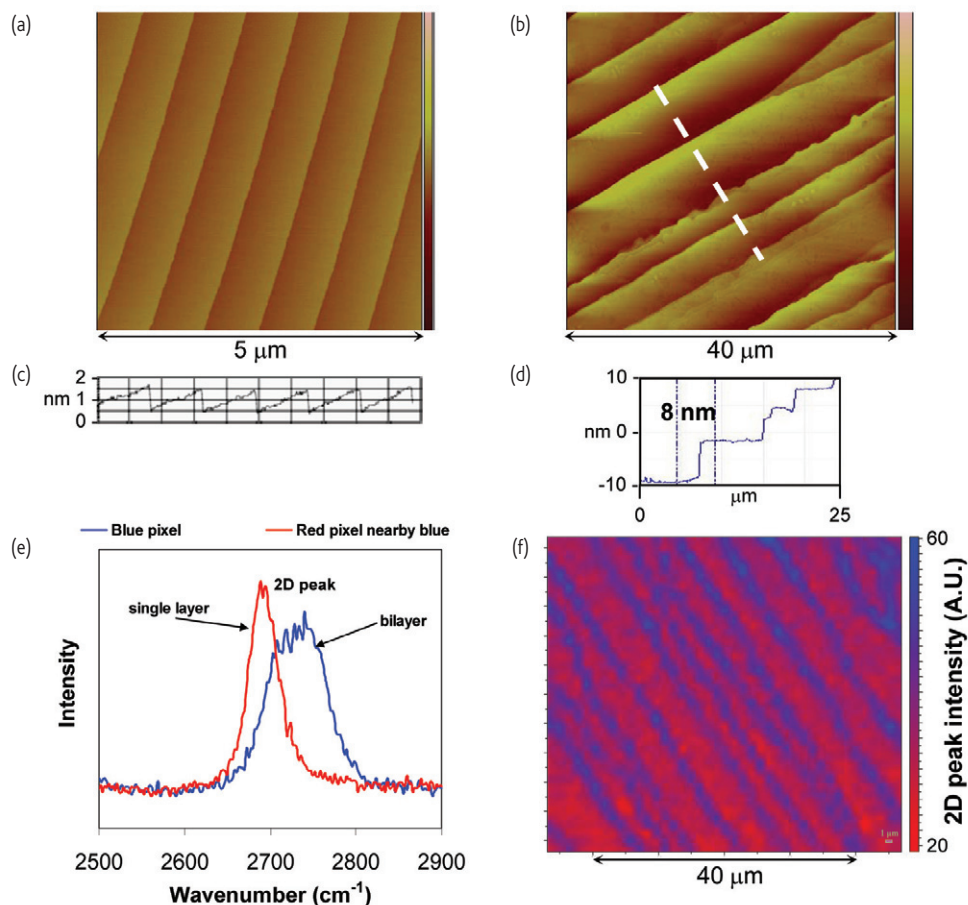

Fig. 3 (a) Non-contact AFM height image of a H$_2$ etched vicinal surface of SiC(0001) after annealing for 20 min at 1555 °C under H$_2$ flow at a pressure of 76 Torr. The z-scale is 10 nm. (b) AFM height image of graphene on a pit-free SiC surface grown at 1575 °C for 30 min under Ar flow at a pressure of 76 Torr. The SiC was H$_2$ etched before graphenization. The z-scale is 15 nm. (c) AFM cross section from left to right edge of image in (a). (d) AFM cross section along the white dashed line in (b). (e) Plots of the 2D Raman peak of graphene. The narrow red peak corresponds to a red/pink pixel in (f) and is associated with one monolayer of graphene, while the much wider blue peak corresponds to a nearby blue pixel in (f), and is associated with two graphene layers. (f) Raman spectroscopy map of the graphene 2D Raman peak intensity distribution over a 55 × 55 μm^2 area. The vast majority of the sample exhibits 2D peak intensity around 30 A.U. (red/pink in the color scale bar) attributed to one graphene layer, while there are stripes of blue (intensity in the range of 60 A.U.) associated with terrace edges and attributed to a graphene bilayer (from reference[55]).

bunching (see increased step heights in Fig. 3d vs. Fig. 3c). These results link the process of graphene formation to step bunching. The H_2 etched surface (Figs. 3a and 3c) shows very limited step bunching when graphene is not allowed to form, although H_2 etching took place just 20 °C below the graphenization step. The Raman spectroscopy map depicted in Fig. 3f is a two-dimensional plot of graphene's Raman 2D peak intensity distribution. The vast majority of the sample (red/pink area) exhibits intensity that is about half that of the blue stripes associated with terrace edges. Based on the plots of Fig. 3e, in which the narrow red peak corresponds to a red/pink pixel in Fig. 3f and the much wider, higher intensity blue peak to a nearby blue pixel in Fig. 3f, red areas correspond to one graphene layer, while blue areas correspond to two graphene layers. The growth of the second graphene layer is initiated at the SiC terrace edges, in agreement with earlier observations[44].

The surface morphology and electrical properties of graphene grown on h-SiC(0001) depend on the miscut angle of the wafer surface[53]. Graphene grown on wafers with miscut angle above 0.28° that have substantially narrower vicinal terraces than graphene on surfaces with miscut angles below 0.1°, shows substantially lower Hall mobility than the latter. Steps impede carrier transport[57] and samples consisting of flat, step-free areas with dimensions larger than the carrier mean free path enable the attainment of the highest mobility of a particular graphene film within its surroundings[53]. Riedl et al.[58], and other groups, demonstrated that annealing epitaxial graphene on SiC(0001) at temperatures up to 700 °C in H_2 breaks the covalent bonds between the buffer layer and the top bilayer of SiC, converting the former to graphene. This reduces dramatically the n type doping of graphene on SiC(0001)[58], and the strong dependence of the mobility of graphene on temperature[59].

Growth on the C-face of hexagonal SiC, e.g., 4H(000$\bar{1}$), exhibits faster kinetics, making thickness control difficult. The number of graphene layers in the resulting multilayer film is not uniform, the surface is wrinkled, and the LEED patterns indicate a large variability in the azimuthal orientation of the graphene film components (layers or domains). Fig. 4 shows LEED patterns taken from two different samples of graphene on 4H–SiC(000$\bar{1}$). Fig. 4a is from a film with average thickness of four graphene layers[60]. Figs. 4b and 4c are from the same spot on a sample with similar average thickness[61]. While there are strong graphene spots corresponding to a graphene unit cell rotation of 30° relative to the SiC cell, as with graphene on SiC(0001), there is also azimuthal disorder in both films, demonstrated by the diffuse arches attributed to graphene. The rotationally disordered graphene has a preferred azimuthal orientation, which, however, is different in the two samples. Fig. 4a shows a maximum intensity in the diffuse arches at ± 2.2° from the SiC [1000] crystallographic direction (rotation of 30° ± 2.2° relative to the strong graphene spot), while in Fig. 4b this angle was between 8° and 9° (rotation of 30° ± 8° to 9°). Apparently, these preferred azimuthal twist orientations depend on sample preparation conditions. Theory has shown that twist angles of 30° ± 8.2° and 30° ± 2.2° produce
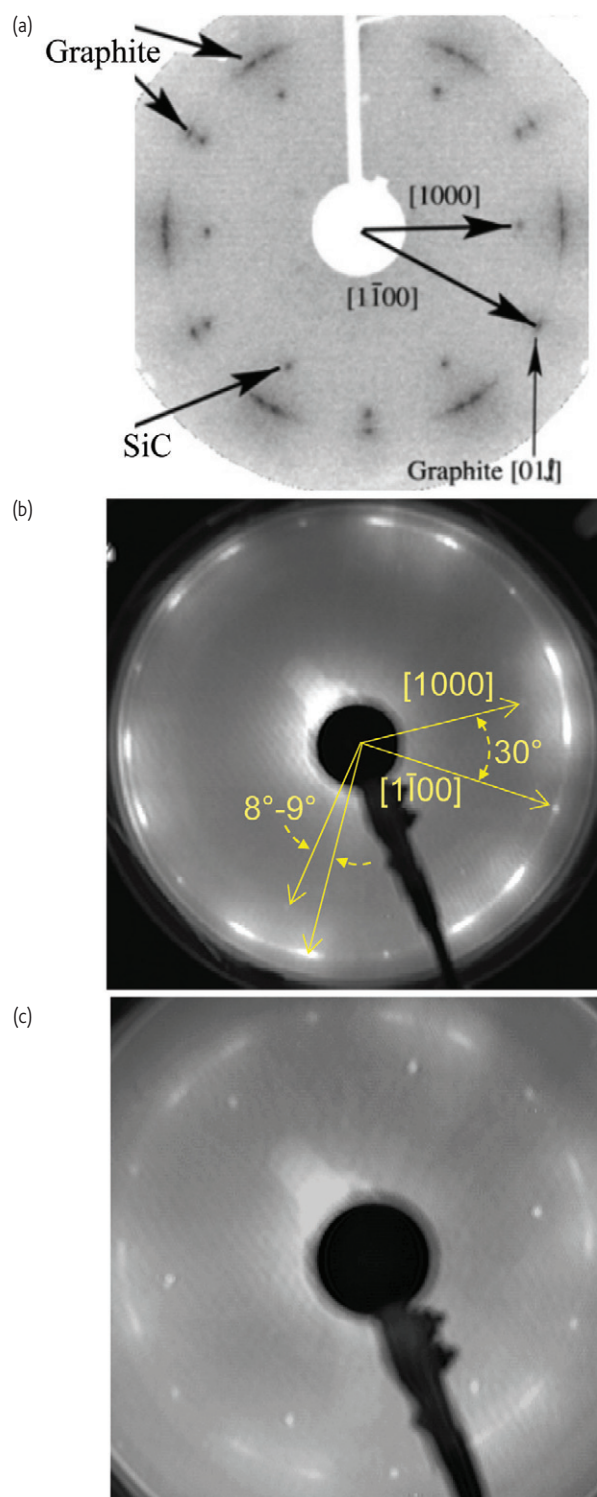

Fig. 4 LEED patterns taken from two different samples, of graphene on 4H–SiC(000$\bar{1}$) with average thickness of four graphene layers. (a) LEED pattern recorded at 103 eV. Reprinted from[60] with permission from Elsevier. (b) and (c): LEED patterns recorded at 76 and 135 eV, respectively from the same spot on another sample (from references[55,61]). (c) was added to show clearly the relative position of graphene and SiC spots, as the latter were faint in the lower energy LEED image in (b).

commensurate structures with the smallest crystalline unit cells (see refs. 62 and 63, and references therein).

In addition to high quality graphene synthesis, another key material issue encountered in the fabrication of graphene devices involves finding an appropriate gate dielectric insulator and substrate. Ideally, a very thin and high dielectric constant film is needed. Graphene is both inert and hydrophobic. Therefore, polar insulators (such as SiO_2, HfO_2, Al_2O_3, etc.) form poor quality, non-uniform and leaky thin films on it. Most importantly, the interaction between graphene, the insulator surface, and the charged defects trapped at or near their interface drastically reduce the mobility of carriers in graphene[64]. A number of different approaches have been used to address this problem, including first depositing a thin, inert buffer layer that wets the surface[64] followed by atomic layer deposition (ALD) of the main film, plasma-assisted deposition of Si_3N_4[65], or deposition of a thin metal film (usually Al) seed layer, which is then *in situ* oxidized prior to ALD of the insulator film[66]. Another approach involves the deposition of graphene on thin layers of exfoliated, single crystal, hexagonal boron nitride (BN) flakes, which can be used both as the gate insulator and as the substrate[67]. This approach provides the minimum perturbation of the excellent intrinsic graphene properties. However, in its current form BN cannot be readily adapted for technological use.

Graphene electronics

Graphene has some outstanding physical properties that make it extremely appealing for applications in electronics. Among these, the extraordinarily high carrier mobility, μ, has received most attention. Mobilities in excess of 100 000 $cm^2/V·s$[68,69] and saturation velocities of about 5×10^7 cm·s^{-1} have been reported[70]. In addition, the thinness, mechanical strength, and flexibility of the material, the fact that it has a very high current carrying capacity (up to $10^9 A/cm^2$), the high thermal conductivity (up to 5000 Wm^{-1} K^{-1})[71], all contribute to its appeal. However, most of these record properties refer to a pristine material under somewhat idealized conditions. In technology, graphene is part of a more complex structure, and under conditions that are dictated by the application itself. For example, electrical transport is subject to a variety of scattering interactions[72-77] . These include scattering through long-range interactions with charged impurities on graphene or more likely at the supporting insulator substrate, short-range interactions with neutral defects or adsorbates and by roughness and phonons. Which mechanism dominates the scattering depends on the quality of the graphene itself and the characteristics of the environment in which the graphene exists[78]. For instance, Coulomb scattering from charged impurities typically dominates at low temperatures when graphene is in contact with polar substrates such as SiO_2 or Al_2O_3[74]. Due to the presence of absorbates, scattering is also present when the substrate is removed and the graphene is suspended. When this graphene is heated, and the adsorbates are volatilized, phonon scattering becomes dominant, making high mobilities attainable[68,69]. When the graphene

is defective, scattering from neutral point defects will dominate carrier transport[79]. The type of scatterer that dominates in a particular graphene sample could be inferred from the magnitude of the carrier mobility (μ), and its dependence on temperature (T) and carrier density (n)[78]. Hence, mobilities greater than 100 000 cm^2/Vs indicate that scattering is dominated by acoustic phonons, where $\mu_{AC} \propto 1/nT$[68,69,74]. Long-range Coulomb scattering results in mobilities on the order of $1000 – 10 000$ cm^2/Vs that are independent of n[73,75,76]. Neutral defects become important in either highly defective samples or at high carrier densities and $\mu_{SR} \propto 1/n$[72,76,80,81].

While the graphene channel may have excellent electrical properties, transport in a graphene device may be strongly affected or even dominated by what happens in other parts of it. Specifically, carriers have to be injected into the graphene channel and then collected through metal contacts. Contacts generate potential energy barriers for carriers that have to be circumvented and thus strongly affect the device performance. Graphene and metal typically have different work-functions, which causes charge transfer (CT) between them. The resulting dipole layer leads to the doping of graphene underneath the metal and a local band-bending. In more reactive metals there is also significant modification of the graphene bandstructure. A carrier injected into graphene must pass both the dipole barrier formed by CT and the metal doped to undoped channel graphene (p-n junction-like) barrier[82-84]. Experiments show that the gate-dependent metal-graphene contact resistance ranges from a couple hundred $\Omega \times \mu m$ to several $k\Omega \times \mu m$[84]. Therefore, contact resistances are comparable to the resistance of the graphene channel itself and their importance in affecting transport is amplified as the channel length is scaled down[85]. Another important consequence of the CT at contacts is the introduction of asymmetry between electron and hole transport[86,87].

Graphene transistors

Once the carriers have been injected into the graphene channel their transport can be controlled by a gate-induced electric field. A negative bias applied to the gate raises the electron energy, while a positive bias lowers it. In ambipolar graphene, when E_F is below the neutrality point E_{NP} (also referred to as the Dirac point), transport involves holes, while for $E_F > E_{NP}$ electrons are transported. As the Fermi energy is changed by the gate, the density-of-states (DOS) and correspondingly the carrier density ($E_F \propto \sqrt{n}$) is changed. This is the basis of 'switching' in graphene field effect transistors (GFETs). However, unlike transistors made of conventional semiconductors with a bandgap, a GFET does not turn off completely, even though DOS = 0 at the neutrality point. A residual conductivity of the order of $G_{min} \approx 4e^2/\pi h$ remains[2]. This is a critical factor that determines what role graphene could play in electronics. The current on off ratio that can be achieved by gating of a graphene transistor is of the order of 10, the exact number depending on the quality of graphene and the effectiveness of the gating. Digital transistors utilized in logic applications, on the other hand, require on/off

ratios higher than about 10^4. It is therefore clear that 2D graphene is not appropriate for a digital switch. There are many research efforts aimed at opening a gap in graphene, but properly addressing this topic goes beyond the scope of this article.

While the lack of a band-gap does not support its use as a digital switch, its outstanding carrier mobility, the high transconductance of graphene devices, and the ultimate thinness and stability of the material make it an excellent candidate for fast analog electronics, specifically radio-frequency (RF) transistors. In analog RF operation the ability to completely switch-off the device, although desirable, is not essential. For example, in signal amplifiers, a major application of these devices, the transistor is in the on-state and the RF signal to be amplified is superimposed on the DC gate bias. In Figs. 5a and 5b we illustrate the structure of typical GFET devices.

A key performance metric for RF transistors is their cut-off frequency, f_T, which is defined as the frequency at which the current gain becomes one when the drain is short-circuited to the source. In a well behaved device f_T is given by $f_T = g_m/2\pi C$, where g_m $(g_m = dI/dV_g)$ and C are the dc transconductance and capacitance of the device, respectively[70,88]. Therefore, optimization of f_T in GFETs involves increasing g_m and minimizing the capacitance. While the cut-off frequency provides an important indicator of the potential of the channel material, voltage gain is usually demanded from actual devices. The voltage gain of a transistor is defined as the ratio of the output voltage (at the drain) to the input voltage (at the gate). It is given by the ratio of the transconductance g_m and the output conductance g_d $(g_d = dI/dV_d)$. In many applications power gain is required and the appropriate metric is the maximum frequency,

f_{max}, which is the frequency at which the unilateral gain becomes unity. Unlike f_T, this metric is strongly dependent not only on the material (graphene), but also on the actual structure of the device.

Graphene exfoliated from graphite has been used successfully to make initially DC[89,90] and latter RF[91-98] GFETs. The first technologically relevant efforts utilizing graphene synthesized on a large (wafer) scale were based on the thermal decomposition of SiC[92,95]. A highly encouraging result came in 2010 when wafer scale RF GFET were produced with f_T values of 100 GHz[95]. However, the lack of a band-gap and the high optical phonon frequency in graphene (~200 meV) made current saturation hard to achieve and thus kept f_{max} low. The fact that the graphene used initially had a rather modest mobility of ~1500 cm^{2}V^{-1}s^{-1} and the gate length was, by today's industry standards, long (240 nm), suggested that drastic improvements in performance could be achieved by subsequent material and device optimizations. Indeed, the second generation of SiC-based GFETs has reached f_T values exceeding 300 GHz with 40 nm channel lengths[97]. Moreover, better current saturation and thinner gate oxides have already produced an improved f_{max} of ~40 GHz. In Fig. 5c we show the frequency dependence of the current gain ($|h_{21}|$) of two different types of GFETs. One is based on CVD graphene on DLC and has a $f_T = 155$ GHz[98] and the other is based on epi-graphene and has a $f_T = 300$ GHz[97].

The development of CVD graphene, which can be transferred onto any substrate also has provided the opportunity of a wide selection of substrates. The commonly used SiO$_2$ is hydrophilic and prone to containing charged defects, both of which substantially degrade the value and reproducibility of the mobility in *GFETs*. One substrate that has been
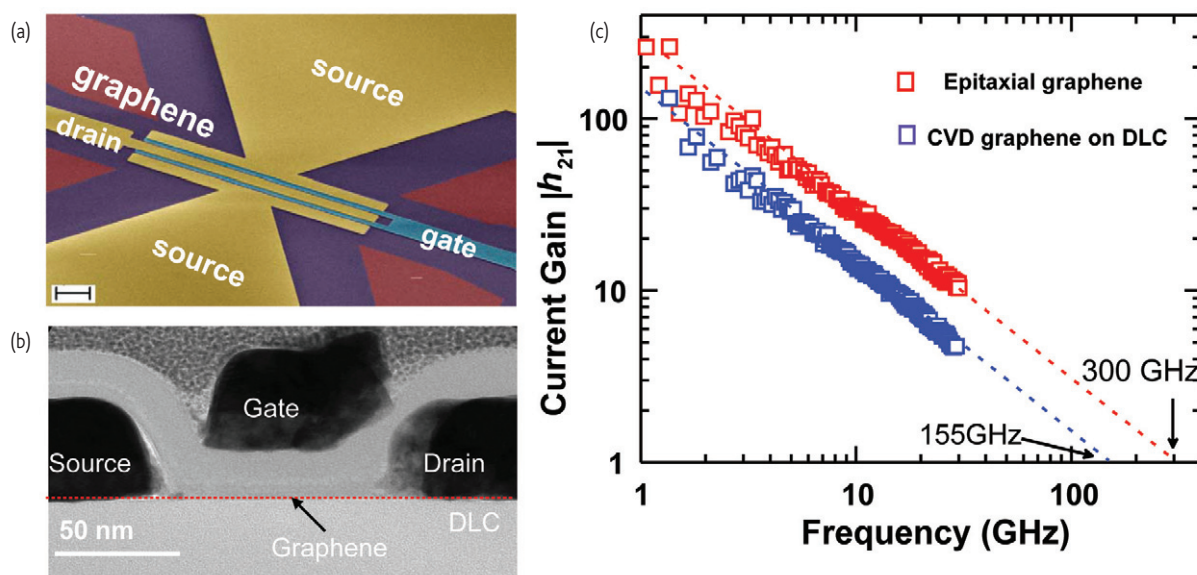

Fig. 5 (a) Optical microscope image of a radio-frequency graphene field-effect transistor (RF GFET). (b) Cross-sectional transmission electron microscope (TEM) image of a GFET. (c) Performance characteristics of GFETs: Plot of current gain (h$_{21}$) versus operation frequency of two different GFETs. One (blue squares) is based on CVD-grown graphene which was transferred to a diamond-like carbon (DLC) substrate and has a cut-off frequency ($|h_{21}| = 1$), f$_T$ = 155 GHz (from reference[98]), and the other (red squares) is based on epitaxially grown graphene and has a f$_T$ = 300 GHz (from reference[97]).

used successfully is diamond-like carbon (DLC). It is fully compatible with graphene, readily available, hydrophobic, and non-polar. The first results yielded *GFETs* with f_T = 155 GHz[98] and more recently improvements have led to f_T =300 GHz [97]. A study of the temperature dependence of GFETs on DLC showed that the performance remains essentially the same from 300 K down to 4 K indicating the absence of carrier freeze-out and demonstrating that graphene electronics could be used in extreme environments such as in outer space. Thin layers of exfoliated, single crystal, hexagonal boron nitride (BN) have been used most successfully both as the gate insulator and as the substrate for graphene transistors[67]. BN is an isomorph of graphite with a large bandgap ($\approx$ 6 eV) making it an ideal choice insulator. Single layer graphene on this material shows enhanced carrier mobilities (~60 000 $cm^2V^{-1}s^{-1}$ at n $\approx$ 1 $\times$ $10^{12}cm^{-2}$) and reduced doping[67]. This would be an ideal material to build graphene devices provided that a fabrication process other than BN single crystal exfoliation, such as CVD BN, can be developed.

Efforts to address integration issues are also on-going. A number of technological issues need to be addressed, primarily involving adapting the deposition technologies developed for silicon technology to graphene. The first monolithically integrated graphene circuit involved a GHz frequency mixer based on epitaxially grown graphene[99]. Mixing was achieved by channel resistance modulation and applied to unipolar (doped) graphene samples. The structure and performance of this frequency mixer are shown in Fig. 6. This IC demonstrated the advantage that graphene offers to such applications because of the insensitivity of the resulting mixer performance to temperature variations. Frequency mixing based on the ambipolar behavior of graphene has also been successfully demonstrated[101]. A key application of analog transistors involves RF signal amplification. Graphene-based IC voltage amplifiers have been fabricated[101] but only moderate power gains (3 dB) have been achieved so far[101]. Efforts to achieve better current saturation and thus increase gain are currently the focus of much effort.
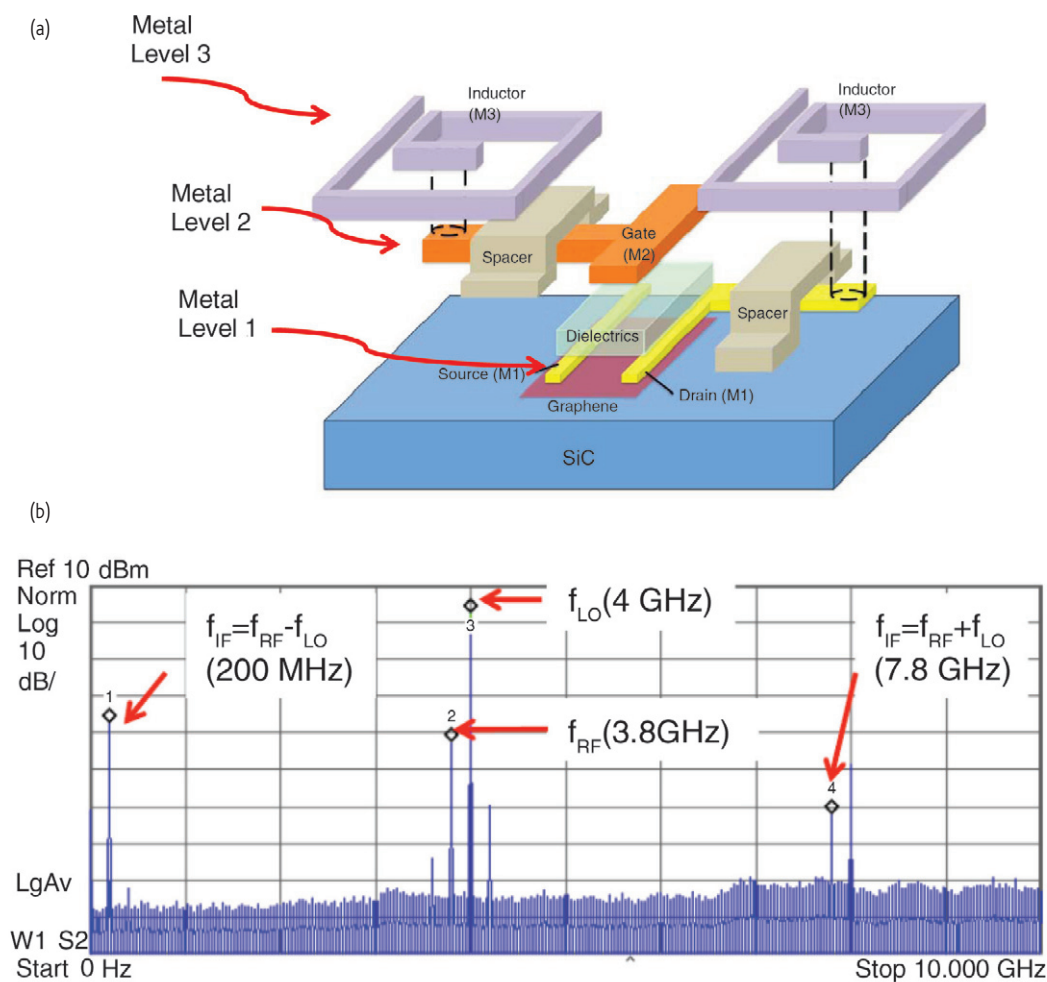

Fig. 6 (a) Schematic illustration of a graphene mixer integrated circuit (IC). The key components include a top-gated graphene transistor and two inductors connected to the gate and the drain of the GFET. Three distinct metals layers of the graphene IC are represented by M1, M2, and M3. A layer of 120 nm thick SiO$_2$ is used as the isolation spacer to electrically separate the inductors (M3) from the underlying interconnects (M1 and M2). (b) Output spectrum of the mixer between 0 and 10 GHz using an input RF frequency, f$_{RF}$ = 3.8 GHz and a local oscillator frequency, f$_{LO}$ = 4 GHz. Each x and y division corresponds to 1 GHz and 10 dB, respectively. The input RF power was adjusted to 0 dB with respect to the RF input. The frequency mixing is observed as two peaks (f$_{IF}$) at 200 MHz and 7.8 GHz (from reference[99]).
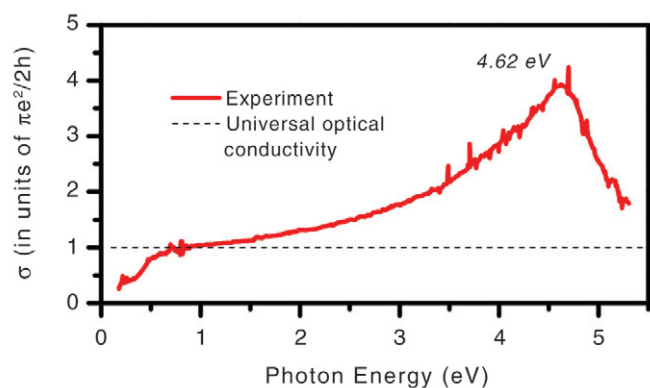
Fig. 7 Optical conductivity (solid line) and "universal" optical conductivity (dashed line) of monolayer graphene in the spectral range of 0.2 – 5.5 eV. The experimental peak energy is 4.62 eV. The deviation of the optical conductivity from the universal value at low energies is attributed to the doping of the sample. Reprinted with permission from[106]. © 2011 by the American Physical Society.

Graphene photonics

In addition to its outstanding electrical transport properties, graphene has unique and tunable optical properties over a wide wavelength range. Moreover, the large wavelength of the light makes these properties less dependent on local defects and the technological use of graphene easier.

Theory based on the independent particle description of graphene predicts an optical absorption for normal incidence photons in the energy range where the dispersion of the Dirac cone is linear, i.e. in the near infrared and early visible, a value of $\pi\alpha$, where α is the fine structure constant ($e^2/\hbar c \approx 1/137$)[102,103]. Indeed, several studies verified that the absorption is about 2.3 %[103-105]. More recently, wide energy range studies of graphene absorption[106,107] reveal a richer behavior. As seen from Fig. 7[106], at energies above the infrared the absorption increases steadily, peaks at about 4.6 eV and has a very asymmetric lineshape.
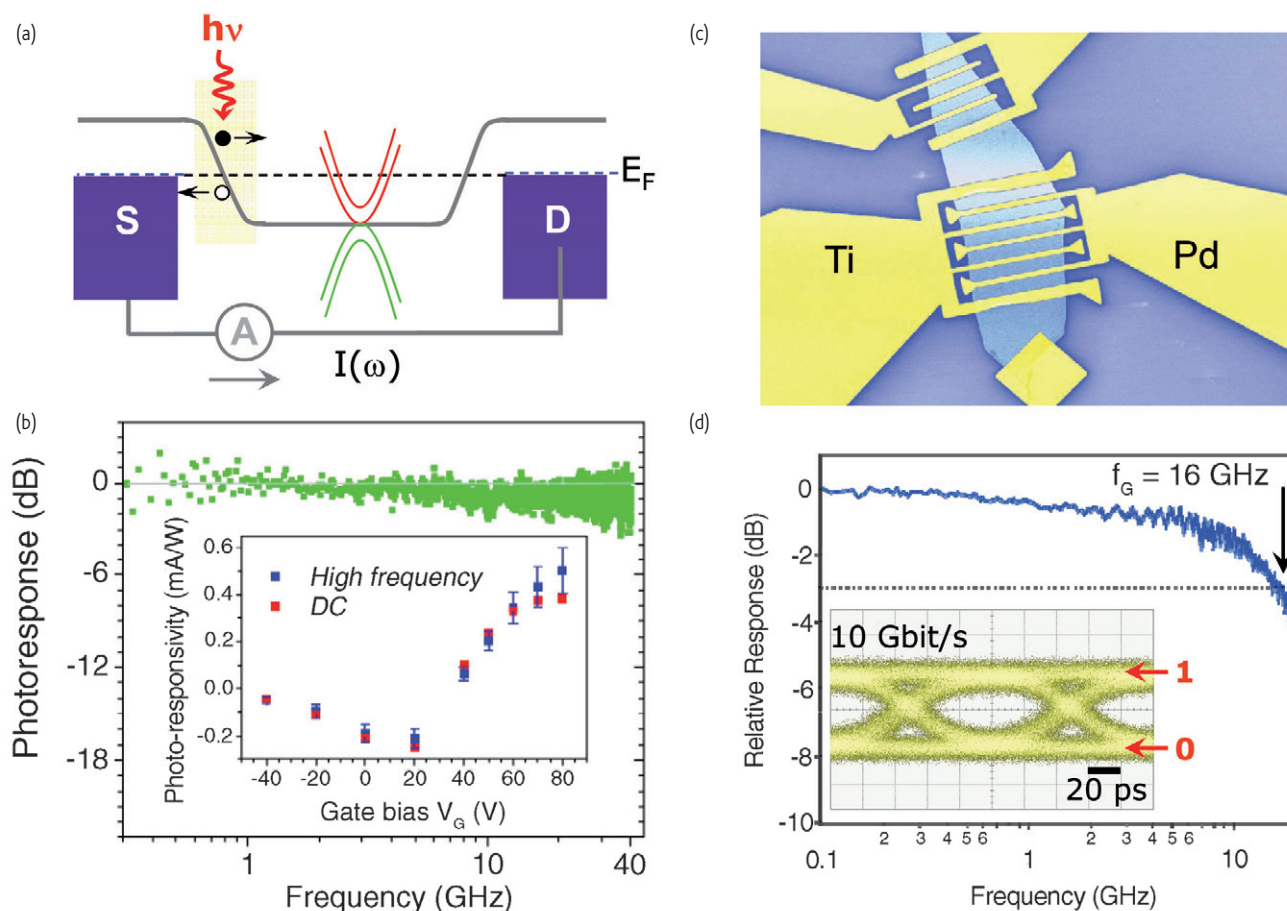

Fig. 8 (a) Schematic of the potential energy profile of a bi-layer graphene FET illustrating the generation of a photocurrent upon illumination near one of the contacts. No source-drain bias is applied. (b) Relative a.c. photoresponse S_{21} of a single contact photodetector as a function of the light intensity modulation frequency up to 40 GHz ($S_{21} = 20\log_{10}R_{a.c.}$ and $R_{a.c.} = \Delta I_{ph}/\Delta P_{in}$ (amp/watt)). The response starts from 0 dB. A response degradation of about 1 dB is observed at 40 GHz, which is caused by the microwave probes. Inset: Peak d.c. and high-frequency (a.c.) photoresponsivity as a function of gate bias. (c) Interdigitated electrode photodetector based on two different metals: a high workfunction (Pd) and a low workfunction (Ti). This configuration allows enhanced photocurrent generation with full device illumination. (d) Relative photoresponse versus the light intensity modulation frequency of an interdigitated electrode photodetector. The 3 dB bandwidth of this photodetector is about 16 GHz. Inset: receiver eye-diagram obtained using the photodetector, showing a completely open eye. Scale bar, 20 ps (from references[123,124]).

This is the range where π–π* interband transitions at the saddle-point singularity near the M point of the graphene Brillouin zone are expected. However, ab-initio GW calculations predict this transition at 5.2 eV[108]. These observations can be accounted for by invoking strong electron-hole interactions to form a saddle-point exciton that red-shifts the excitation energy. The asymmetric lineshape develops through a Fano-type interaction between this exciton and the continuum of interband transitions near the M point[106-109].

The excited states of graphene decay very fast. An initial ultrashort pulse generates e-h pairs in a highly non-equilibrium state. Electronic interactions, i.e., Coulombic carrier-carrier interactions provide a very fast energy redistribution mechanism[110,111]. Time-resolved measurements show that after about 200 − 300 fs a Fermi-Dirac distribution is attained with an elevated electronic temperature T_e[109]. As expected, this electronic decay rate is a function of the electron density (doping). Along with the energy redistribution processes, energy dissipation takes place via phonon emission. The decay via optical phonons is fast, taking place on a few picosecond time scale. Once, however, the excitation energy has fallen below the optical phonon energy (about 200 meV), acoustic phonon emission is very slow (nanoseconds) and this leads to the formation of an energy dissipation bottleneck[111]. Due to this uncoupling of lattice and electronic temperatures, the resulting "hot" electrons can persist for nanoseconds. Coupling of the electrons with a polar substrate's surface phonon polariton modes (SPP) may become an important decay path in this case[112].

In the presence of a field gradient, photoexcitation of graphene produces a photocurrent, which could be used in a number of optoelectronic applications. The advantages of using graphene as a photodetector are the wide absorption range, the high mobility of carriers, the thinness and low cost of the material and the ability to operate at ambient temperature. The electric field can be produced by applying a voltage bias. However, since graphene does not have a band-gap, this would produce a sizeable dark current, leading to heating and excessive shot and thermal noise. For these reasons, the use of internal fields is desirable. Such fields are already present at graphene p-n junctions. Such junctions are formed by, for example, fabricating split-gate devices, or are formed naturally at metal-graphene contacts due to the difference between their work functions and the resulting charge transfer (see Fig. 8a). The carriers are driven by the potential gradient at the p-n junction[113-115] and by photothermal effects[116-118], which can arise because of laser heating and the difference in Seebeck coefficients of the two sides, $V_{PTE} = (S_2 − S_1)\Delta T$. The photothermal effects are enhanced due to the acoustic phonon bottleneck leading to "hot" carriers. It was suggested that the generated current signal in the latter case can still be fast, because $T_e > T_{lattice}$ and heat transport involving electronic carriers, which have a much lower heat capacity than that of phonons[117,118].

In the above we focused on the spectral properties of graphene arising from interband transitions. In the far-IR and terahertz regions,
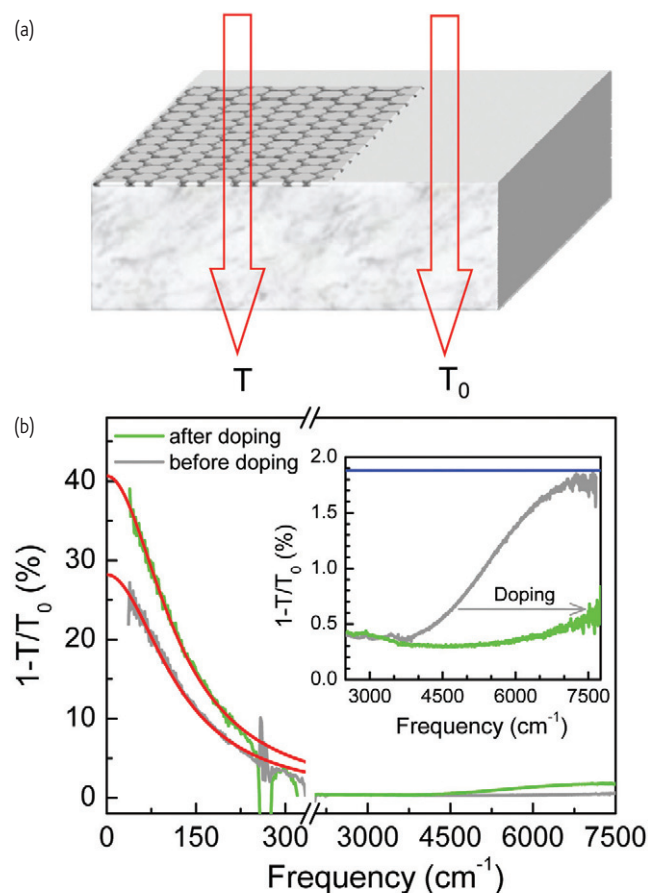

Fig. 9 (a) Schematic of the way the infrared spectra of CVD graphene transferred on a quartz substrate are obtained. (b) Near infrared and far-infrared (Drude) absorption spectra of CVD graphene as transferred (black curve) and after doping (green). Fit to Drude model is shown in red. Inset: The effect of doping graphene with $(C_2H_5)_3OSbCl_6$. The blue line shows the universal absorption on quartz (from reference[119]).

however free carrier absorption dominates. The frequency dependence of free carrier response in graphene can be adequately described by the Drude model of metallic absorption with the dynamical conductivity given by $\sigma(\omega)=iD/[\pi(\omega+i\Gamma)]$, where D is the Drude weight and Γ^{-1} is the carrier scattering rate[119]. Fig. 9 shows mid- and far- infrared spectra of CVD graphene and the different effect that chemical (or electrostatic) doping has on these two regions of the graphene spectrum. Analysis of the light extinction $(1−T/T_0)$ in the Drude regime can provide the optical conductivity, the degree of doping of graphene and even the carrier mobility[119].

In addition, the single particle excitations of graphene, its collective excitations, i.e., surface plasmons (SP), are interesting and of technological importance. Unlike the linear dispersion of the quasi-particles in graphene, the SPs have a quadratic dispersion and are not excited directly by light[120]. However, SP excitation is possible upon breaking the symmetry of the graphene. This can be easily accomplished by patterning graphene lithographically, to generate 1D or 0D structures[120]. While plasmonics

based on noble metal nanoparticles is a highly active and rapidly advancing field , graphene offers new opportunities and advantages in plasmonics. These are associated with the extreme confinement in graphene, the significant longer SP lifetimes[121] and hence long propagation distances and, most importantly, the unique ability to tune the carrier density in graphene electrostatically or chemically. In these patterned graphene structures strong light-graphene coupling would be used to manipulate its optical properties.

Optoelectronic applications

The first demonstration of a graphene photodetector was based on the fields generated at metal-graphene contacts. Short segments of graphene (~200 nm) were contacted with Pd and irradiated by light in the visible and IR[123]. Fig. 8b shows the measured AC photoresponse of a single junction detector to a 1.55 μm modulated light beam. A nearly constant response is observed up to 40 GHz, which was the frequency limit of the measurement system. Modeling suggested that eventually the detector response will be limited by the RC constant of the devices to about 0.6 THz. In a symmetric device, simultaneous illumination of both contacts produces equal but opposite polarity currents and therefore no net photocurrent. An improved design shown in Fig. 8c provides a significantly increased photoresponse and allows photodetection with full surface illumination (Fig. 8d). This device utilizes inter-digitated metal electrodes made of two different metals, one with a high workfunction and the other with a low workfunction. These two different workfunctions produce different doping and band-bending in graphene that allows photodetection over the entire area of the device. Photodetectors of this design were shown to reliably detect optical data streams of 1.55 μm light pulses at a rate of 10 GBits/s[124] .

To further increase the photoresponse of graphene detectors, a number of other approaches have been employed. In one case, enhanced light absorption and photocurrent generation was achieved through excitation of the plasmons of gold nanoparticles deposited on graphene[125]. While another involves incorporating graphene inside a planar Fabry-Pérot microcavity increasing its absorption to about 60 % at 850 nm[126].

The ability to modulate the Fermi level of graphene by a gate field naturally leads to its application as a fast electro-absorption modulator[127]. High speed, small footprint and high bandwidth modulators are highly desirable for on-chip optical interconnects. However, although the light-graphene interaction is strong, the absorption of a light beam by a single graphene layer is insufficient. M. Liu *et al.*[127] coupled the graphene with a silicon waveguide to increase the absorption and achieved a modulation by 0.1 dBμm^{-1} of 1.35 − 1.60 μm light at frequencies over 1 GHz. As in the case of photodetectors, an important advantage of graphene-based modulators over conventional III-V based devices is the ability to be integrated with Si-CMOS electronics.

Another useful optical property of graphene is its saturable absorption. Saturable absorption describes the situation where light absorption decreases with increasing light intensity. Most materials show some saturable absorption but, typically, at very high light intensities (close to the optical damage). Saturable absorbers are used in laser cavities to convert the continuous wave output of a laser into a train of ultrashort light pulses**.** Graphene with its wide absorption range, fast decay and high stability is well suited for this application and indeed it has been successfully used to produce picosecond laser pulses[128,129].

Conclusions

In this review we have presented some of the recent progress in graphene synthesis and applications in electronics and photonics. The research in this area is still in an early development stage and much more work is needed to realize graphene's technological potential. It is already clear, however, that applications of graphene in radio-frequency electronics, flat panel displays, and photovoltaic cells as transparent conductive electrodes, and high current density conductors are very promising. Similarly, graphene photodetectors and imaging systems, light modulators and switches, mode locking devices, rf radiation screening systems, and 2D graphene plasmonics applications can be quite competitive. At the same time, the quality and area of synthetic graphene is continually improving. We should expect many other applications that exploit the unique properties of graphene to appear in the coming years. Success will require a persistent, multidisciplinary research effort and sufficient funding.

REFERENCES

1. Wallace, P. R., *Phys Rev* (1947) **71**, 622.
2. Castro Neto, A. H., *et al.*, *Rev Mod Phys* (2009) **81**, 109.
3. Geim, A. K., and Novoselov, K.S., *Nat Mater* (2007) **6**, 183.
4· Fuhrer, M. S., *et al.*, *MRS Bulletin* (2010) **35**, 289.
5. First, P. N., *et al. MRS Bulletin* (2010) **35**, 296.
6. Avouris, P., *Nano Let* (2010) **10**, 4285.
7. Allen, M. J., *et al.*, *Chem Rev* (2010) **110**, 132.
8. Das Sarma, S., *et al.*, *Mod Phys* (2011) **83**, 407.
9. Novoselov, K. S., *et al.*, *Science* (2004) **306**, 666.
10. Hagstrom, S., *et al.*, *Phys Rev Lett* (1965) **15**, 491.
11. Morgan, A. E., and Samorjai, G. A., *Surf Sci* (1968) **12**, 405.
12. May, J. W., *Surf Sci* (1969) **17**, 267.
13. Shelton, J. C., *et al.*, *Surf Sci* (1974) **43**, 493.
14. Grabke, H. J., *et al.*, *Surf Sci* (1977) **63**, 377.
15. Hamilton, J. C., and Blakely, J. M., *Surf Sci* (1980) **91**, 119.
16. Ohla, K., and Grabke, H. J., *Werkst Korros* (1982) **33**, 341.
17. Angermann, H.-H., and Hörz, G., *Appl Surf Sci* (1993) **70/71**, 163.
18. Zhang, Y., *et al.*, *Phys Chem Lett* (2010) **1**, 3101.
19. Yu, Q., *et al.*, *Appl Phys Lett* (2008) **93**, 113103.
20. Reina, A., *et al.*, *Nano Lett* (2009) **9**, 30.
21. Land, T. A., *et al.*, *Surf Sci* (1992) **264**, 261.

22. Li, X. S., *et al., Science* (2009) **324**, 1312.
23. Chen, S., *et al., Nano Lett* (2011) **11**, 3519.
24. Cai, W. W., *et al., Nano Res* (2009) **2**, 851.
25. Marchini, S. S., *et al., Phys Rev B* (2007) **76**, 075429.
26. Sutter, P. W., *et al., Nature Mat* (2008)**7**, 411.
27. N'Diaye, A. T., *et al., Phys Rev Lett* (2006) **97**, 215501.
28. Coraux, J., *et al., Nano Lett* (2008) **8**, 565.
29. Bae, S. *et al., Nature Nano* (2010) **5**, 574.
30. Kim, K. S., *et al., Nature* (2009) **457**, 706.
31. Huang, P. Y., *Nature* (2011) **469** , 389.
32. Gao, L., *et al., Nano Lett* (2010) **10**, 3512.
33. Walter, A. L., *et al., Phys Rev B* (2011) **84**, 195443.
34. Zhu, Y., *et al., Adv Mater* (2010) **22**, 3906.
35. Li, X., *et al., J Am Chem Soc* (2011) **133**, 2816.
36. Badami, D. V., *Nature*, (1962) **193**, 569.
37. van Bommel, A. J., *et al., Surf Sci* (1975) **48,** 463.
38. Forbeaux, I., *et al., Appl Surf Sci* (2000) **162/163**, 406.
39. Berger, C., *et al., J Phys Chem B* (2004) **108,** 19912.
40. Hass, J., *et al., Appl Phys Lett* (2006) **89**,143106.
41. Tanaka, S., *et al., Phys Rev B* (2009) **80**, 121406R.
42. Tromp, R. M., and Hannon, J. B., *Phys Rev Lett* (2009) **102**,106104.
43. Virojanadara, C., *et al., Phys Rev B* (2008) **78**, 245403.
44. Emtsev, K. V., *et al., Nature Materials* (2009) **8**, 203.
45. Dimitrakopoulos, C., *et al., J Vac Sci Technol B* (2010) **28,** 985.
46. Gaskill, D. K., In *Proceedings of 215th ECS Meeting*, San Francisco, CA, USA (2009).
47. de Heer, W. A., *PNAS* (2011) **108**, 16900.
48. Emtsev, K. V., *et al., Phys Rev B* (2008) **77**, 155303.
49. Hannon, J. B., *et al., Phys Rev Lett* (2011) **107**, 166101.
50. Hannon, J. B., and Tromp, R. M., *Phys Rev B* (2008) **77**, 241404(R).
51. Luxmi, N., *et al., Vac Sci Technol B* (2010) **28**, C5C1.
52. Dimitrakopoulos, C., *et al.,* Extended Abstract, *GraphITA Workshop*, Gran Sasso National Laboratories, Assergi-L'Aquila, Italy (2011).
53. Dimitrakopoulos, C., *et al., Appl Phys Lett* (2011) **98**, 222105.
54. Dimitrakopoulos, C., *et al., 2011 MRS Fall Meeting*, Abstract Viewer, Materials Research Society, Boston, MA, USA, (2011) Program No. AA11. **3**.
55. Dimitrakopoulos, C., *et al., Lawrence Symposium on Epitaxy*, Scottsdale, AZ, (2012).
56. Ramachandran, V., *J Electron Mater* (1998) **27**, 308.
57. Lin, Y.-M., *et al., IEEE Electron Device Lett* (2011) **32**, 1343.
58. Riedl, C., *et al., Phys Rev Lett* (2009) **103**, 246804.
59. Speck, F., *et al., Appl Phys Lett* (2011) **99**, 122106.
60. de Heer, W. A., *et al., Solid State Commun* (2007) **143**, 92.
61. Dimitrakopoulos, C., McArdle, T. J., and Grill A., *unpublished results*.
62. McDonald, A. H., and Bistritzer R., *Nature* (2011) **474**, 453.
63. Luican, A., *et al., Phys Rev Lett* (2011) **106**, 126802.
64. Farmer, D. B., et al., *Nano Lett* (2009) **9**, 4474.
65. Zhu, W., *et al., Nano Lett* (2010) **10**, 3572.
66. Kim, S., *et al., Appl Phys Lett* (2009) **94**, 062107.
67. Dean, C. R., *et al., Nature Nano* (2010) **5**, 722.
68. Bolotin, K. I., *Solid State Commun* (2008) **146**, 351.
69. Du, X., *et al., Nature Nanotech* (2008) **3**, 491.
70. Schwierz, F., *Nature Nano* (2010) **5**, 487.
71. Balandin, A., *Nature Nano* (2011) **10**, 569.
72. Adam, S., *et al., Proc Natl Acad Sci USA* (2007) **104**, 18392.
73. Chen, J.-H., *et al., Solid State Commun* (2009) **149**, 1080.
74. Chen, J.-H., *et al., Nature Nanotech* (2008) **3**, 206.

75. Nomura, K., and MacDonald, A. H., *Phys Rev Lett* (2006) **96**, 256602.
76. Zhu, W., *et al., Phys Rev B* (2009) **80**, 235402.
77. Katsnelson, M. I., and Geim, A. K., *Phil Trans R Soc* A (2008) **366**, 195.
78. Farmer, D. B., *et al., Phys Rev B* (2011) **84**, 205417.
79. Chen, J.-H., *et al., Phys Rev Lett* (2009) **102**, 236805.
80. Ando, T., *J Phys Soc Jpn* (2006) **75**, 074716.
81. Chen, J.-H., *et al., Solid State Commun* (2009) **149**, 1080.
82. Giovannetti, G. P., *et al., Phys Rev Lett* (2008) **101**, 026803.
83. Khomyakov, P. A., *et al., Phys Rev B* (2009) **79**, 195425.
84.   Xia, F., *et al., Nature Nano* (2011) **6**, 179.
85. Wu, Y., *et al., Nano Lett,* doi: 10.1021/nl204088b.
86. Huard, B., *et al., Phys Rev B* (2008) **78**, 121402(R).
87. Cayssol, J., *et al., Phys Rev B* (2009) **79**, 075428.
88. Avouris, P., *et al., Nature Nano* (2007) **2**, 605.
89. Lemme, M. C., *IEEE Electron Device Lett* (2007) **28**, 282.
90. Kedzierski, J., *et al., IEEE Trans Electron Devices* (2008) **55**, 2078.
91. Meric, I., *et al., IEDM Tech Dig* (2008) 1–4.
92. Moon, J. S., *et al., IEEE Electron Dev Lett* (2009) **30**, 650.
93. Lin, Y.-M., *et al., Nano Lett* (2009) **9**, 422.
94. Lin, Y.-M., *et al., IEEE Electron Device Lett* (2010) **31**, 68.
95. Lin, Y.-M., *et al., Science* (2010) **327**, 662.
96. Liao L., *et al., Nature* (2010) **467**, 305.
97. Wu, Y., *et al., IEDM Technical Digest* (2011) **23.8**, 528.
98. Wu Y., *et al., Nature* (2011) **472**, 74.
99. Lin, Y.-M., *et al., Science* (2011) **332**, 1294.
100. Han, W. A., *et al., IEEE Electron Device Lett* (2010) **31**, 906.
101. Han, S.-J., *Nano Lett* (2011) **11**, 3690.
102. Kuzmenko, A. B., *et al., Phys Rev Lett* (2008) **100**, 117401.
103. Nair, R. R., *et al., Science* (2008) **320**, 1308.
104. Mak, K. F., *et al., Phys Rev Lett* (2008) **101**, 196405.
105. Wang, F., *et al., Science* (2008) **320**, 206.
106. Mak, K. F., *et al., Phys Rev Lett* (2011) **106**, 046401.
107. Chae, D. H., *et al., Nano Lett* (2011).
108. Yang, L., *et al., Nano Lett* (2007) **7**, 3112.
109. Malic, E., *et al., Phys Rev B* (2011) **84**, 205406.
110. Kim, R., *et al., Phys Rev B* (2011) **84**, 075449.
111. Bistritzer, R., and MacDonald, A. H., *Phys Rev Lett* (2009) **102**, 206410.
112. Rotkin, S. V., *et al., Nano Lett* (2009) **9**, 1850.
113. Lee, E. J. H., *et al., Nature Nano* (2008) **3**, 486.
114. Xia, F., *et al., Nano Lett* (2009) **9**, 1039.
115. Park, J., *et al., Nano Lett* (2009) **9**, 1742.
116. Xu, X., *et al., Nano Lett* (2010) **10**, 562.
117. Song, J. C., *et al., Nano Lett* (2011) doi: 10.1021/nl202318u.
118. Gabor, N. M., *et al., Science* (2011) **334**, 648.
119. Yan, H., *et al., ACS Nano* (2011) **5**, 9854.
120. Koppens, F. H. L., *et al., Nano Lett* (2011) **11**, 3370.
121. Halas, N., *et al., Chem Reviews* (2011) **111**, 3913.
122. Yan, H., *et al., arXiv*: 1202.5235.
123. Xia, F., *et al., Nature Nano* (2009) **4**, 839.
124. Mueller, T., *et al., Nature Photon* (2010) **4**, 297.
125. Echtermeyer, T. J., *et al., Nature Commun* (2011) **2**, 458.
126. Furchi, M., *et al., arXiv*:1201.3175v1.
127. Liu, M., *et al., Nature* (2011) **474,** 64.
128. Bao, Q. L., *et al., Adv Funct Mater* (2009) **19**, 3077.
129. Sun Z, *et al., ACS Nano* (2010) **4**, 803.